

## Underlying mechanism of dual hysteresis in NiMnGa single crystals

R.F. Hamilton<sup>a,\*</sup>, S. Dilibal<sup>b</sup>, H. Sehitoglu<sup>b</sup>, H.J. Maier<sup>c</sup>

<sup>a</sup> Department of Engineering Science and Mechanics, The Pennsylvania State University, 212 Earth-Engineering Sciences Bldg., University Park, PA 16802-6812, USA

<sup>b</sup> Department of Mechanical Science and Engineering, University of Illinois, 1206 West Green Street, Urbana, IL 61821, USA

<sup>c</sup> University of Paderborn, Lehrstuhl f. Werkstoffkunde, D-33095 Paderborn, Germany

### ARTICLE INFO

#### Article history:

Received 17 August 2010

Accepted 14 October 2010

#### Keywords:

Mechanical characterization  
Strain measurement  
Digital image correlation  
Shape memory alloys  
Martensitic transformation  
Hysteresis

### ABSTRACT

NiMnGa single crystals are compressed in the [001] orientation at room temperature. The stress–strain response exhibits multiple stages as the deformation proceeds. Initially, the response exhibits a stress drop in the stress–strain curve preceding a plateau stress. By contrast, the second transition, which occurs at five times the initial critical transformation stress, produces a work hardening like response. Complete pseudoelastic (PE) recovery ensues upon unloading with the reverse transformation exhibiting the same two-stages. Furthermore, for the dual hysteresis that results, the second hysteresis is nearly four times wider than the first. The underlying transformation path for each stage is ascertained from local strain analysis utilizing variable magnification *in situ* digital image correlation (DIC). We distinguish three different morphological transitions; band formation, phase front propagation, and heterogeneous growth. The morphologies can be attributed to austenite undergoing the successive transitions  $10M \rightarrow 14M$  (modulated to modulated) and  $10M \rightarrow L1_0$  (modulated to non-modulated). Differential critical stress and hysteresis levels are rationalized based on the initial modulated-to-modulated and successive modulated-to-non-modulated transition. The strain–temperature response is reported, as well, and exhibits a tiny thermal hysteresis (5 °C), which is attributed to the modulated-to-modulated conversion.

© 2010 Elsevier B.V. All rights reserved.

### 1. Introduction

The Heusler NiMnGa alloys have attracted attention primarily due to facilitation of magnetic-field induced strains for actuator applications [1–4]. The dependence of the phase transition temperatures on the composition and valence electron number to atom ( $e/a$ ) ratio has been well reported [4,5]. NiMnGa alloys may be divided into three groups [6–8]. At the extremes are alloys with a martensite start temperature  $M_s \leq -73$  °C and  $e/a < 7.60$  and alloys with  $M_s$  greater than 100 °C and  $e/a > 7.70$ . An intermediate group exhibits  $M_s$  closer to room temperature. The stress-induced martensitic transformation (SIMT) from the austenitic state has been reported in a few studies on single crystalline NiMnGa alloys with  $M_s$  close to room temperature [9–11]. The SIMT proceeds via successive inter-martensitic transformations, such that the transitions are  $A \rightleftharpoons 10M \rightleftharpoons 14M \rightleftharpoons L1_0$ . The  $10M$  and  $14M$  refer to five- and seven-layered martensite structures, and the  $L1_0$  is a non-modulated martensite. The crystal structures are extensively described in the literature [5,7,12].

For classes of the NiMnGa alloys in the intermediate group, the isothermal stress–strain response has been investigated for [001] oriented single crystals compressed near room temperature [10,11]. Martynov and Kokorin [10] report only one transition, which exhibits a single hysteresis. Utilizing *in situ* X-ray analysis, they conclude that a single crystal martensite results, which exhibits the five-layered ( $10M$ ) structure. The authors calculate theoretical transformation strains for  $A \rightarrow 10M$  (–4.9%) and  $14M \rightarrow L1_0$  (–0.3%). They conclude that the stress level to induce  $14M \rightarrow L1_0$  cannot be reached prior to fracture. Cui and colleagues [11] observe two-stages in the compressive stress–strain response. The authors monitor the evolution of surface relief of a polished sample throughout loading. Based on optical micrographs, the authors ascertain that the two stages exhibit different characteristics of variant rearrangement; twin boundary motion during the first stage and no twin-boundary in the second.

In order to scrutinize the underlying morphology of the transformation path, the current work measures meso-scale deformation employing *in situ* digital image correlation (DIC). Conventional deformation measurements, i.e. extensometer or crosshead displacement, are considered macro-scale. In this study, the dual hysteresis is investigated in a two-stage transformation observed in the isothermal pseudoelastic response of [001] oriented single crystals loaded in compression at room temperature. The current alloy composition, Ni<sub>53</sub>Mn<sub>22</sub>Ga<sub>25</sub> (at%), is very close to that of Ref.

\* Corresponding author. Tel.: +1 814 865 7684; fax: +1 814865 9974.

E-mail addresses: [rhamilton@psu.edu](mailto:rhamilton@psu.edu) (R.F. Hamilton), [dilibal@illinois.edu](mailto:dilibal@illinois.edu) (S. Dilibal), [huseyin@illinois.edu](mailto:huseyin@illinois.edu) (H. Sehitoglu), [hmaier@mail.uni-paderborn.de](mailto:hmaier@mail.uni-paderborn.de) (H.J. Maier).

[11],  $\text{Ni}_{53.2}\text{Mn}_{22.6}\text{Ga}_{24.2}$  (at%). However, in Ref. [11], the first and the second transformation stress magnitudes ( $\sim 30$  and  $\sim 100$  MPa) are significantly lower than the current results ( $\sim 60$  and  $\sim 400$  MPa). Dual hystereses are also observed in Ref. [11] and the initial and secondary hysteresis magnitudes are approximately 25 and 60 MPa. On the other hand, in this work the dual hysteresis magnitudes are approximately 30 and 130 MPa. The marked differential transformation stresses and hysteresis observed in the current results warrant further investigation. To study the stability of the underlying transformation path, *in situ* DIC analysis is reported after repeated deformation cycling. Furthermore, the influence of the modulated-to-modulated transition on the thermal hysteresis is reported for the strain–temperature response.

## 2. Materials and methods

Single crystal  $\text{Ni}_{53}\text{Mn}_{22}\text{Ga}_{25}$  (at%) alloys were grown using the Bridgman technique in an inert environment. Samples were sectioned into  $4\text{ mm} \times 4\text{ mm} \times 10\text{ mm}$  pieces using a wire electrical discharge machine. The specimens were cut with the [001] direction longitudinally oriented and the (100) plane oriented parallel to a side face. All reported stresses and strains were measured along the [001] direction. Chemical analysis was performed on the material after crystal growth to confirm that no changes in the composition occurred during the growth process. The specimens reported in this paper are not artificially aged and are reported to be in the “unaged” condition.

The stress-free thermal-induced martensitic transformation for the current  $\text{Ni}_{53}\text{Mn}_{22}\text{Ga}_{25}$  composition is characterized using a differential scanning calorimeter (DSC). The DSC thermo-grams show that the  $M_s = 27.5^\circ\text{C}$ . Entel et al. [4] and Planes et al. [5] have summarized the dependence of the transformation phase diagram on the  $e/a$  ratio. For the current  $\text{Ni}_{53}\text{Mn}_{22}\text{Ga}_{25}$  composition, 10M martensite is the thermal induced crystal structure because  $e/a = 7.59$ , and thus, the martensitic transformation is attributed to a transition to the 10M. The influence of stress on the thermal hysteresis is studied. The temperature is cycled for [001] oriented single crystals loaded in compression.

The isothermal stress-induced martensitic transformation is investigated near room temperature. Compressive loading of [001] oriented  $\text{Ni}_{53}\text{Mn}_{22}\text{Ga}_{25}$  single crystals is conducted in strain-control control at a rate of about  $1 \times 10^{-3}\text{ s}^{-1}$ . Macro-scale strain was measured with a miniature extensometer with a 5 mm gauge length. In addition to the MTS extensometer, nominal strains were evaluated from DIC data. Both represent average strain measurements over a 5 mm gauge length. Based on the equivalence of the loading response, the DIC measurements are considered for the remaining analysis.

Within the gauge length, meso-scale strains were calculated utilizing full-field optical digital image correlation. For DIC analysis, the specimen surface was polished and spray-painted with a speckle pattern. *In situ* images of the specimen surface were captured with an IMI model IMB-202FT ( $1600 \times 1200$  pixels) and Sony XCD-sx900 ( $1280 \times 960$  pixels) CCD cameras. Image acquisition was programmed into the mechanical testing software, which is based on National Instruments LabVIEW. Digital images were captured *in situ* at a rate of 1 image per second. Displacements were measured by tracking the evolution of the intensity pattern resulting from deformation of the specimen and the speckle pattern applied to its surface. The basic theory of DIC is expounded on in the works of Sutton et al. [13–15]. The strains were calculated from the displacement gradients. Image correlation and subsequent strain calculations were achieved using software developed by Correlated Solutions ([www.correlatedsolutions.com](http://www.correlatedsolutions.com)). The material is subjected to ten deformation cycles up to the maximum

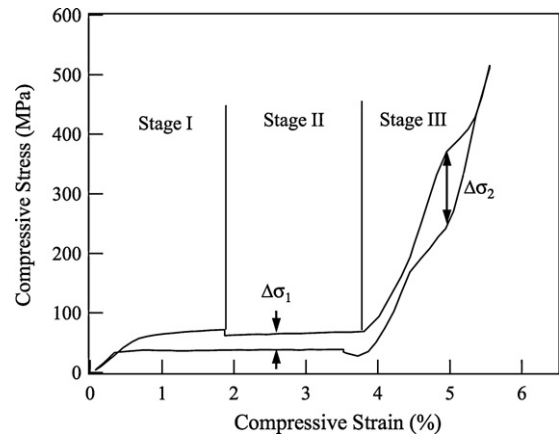


**Fig. 1.** Compressive pseudoelastic response for an unaged  $\text{Ni}_{53}\text{Mn}_{22}\text{Ga}_{25}$  [001] oriented single crystal, which is loaded near room temperature. The dual stress hysteresis are designate  $\Delta\sigma_1$  and  $\Delta\sigma_2$ . The response exhibits three stages based on the evolution of full-field strains in Fig. 2.

transformation strain to ascertain the stability of the underlying transformation path.

## 3. Results and discussion

Fig. 1 shows the nominal compressive stress–strain response of the NiMnGa single crystal near room temperature. The temperature is slightly below the stress-free  $M_s$  temperature ( $27.5^\circ\text{C}$ ). Consequently, the initial microstructure can include a mixture of austenite and a finite volume fraction of self-accommodated martensite. The stress–strain response is envisaged as three stages, which are indicated in Fig. 1. The critical stress in Stage I, measured using a 0.2% offset, is  $\sigma^{\text{cr}1} \approx 60$  MPa. Lüders-like deformation occurs and a stress-peak precedes the plateau. The stress drops from approximately 72 to 62 MPa. Stage II occurs over a stress plateau at 62 MPa. Within Stage III the critical stress magnitude is  $\sigma^{\text{cr}2} \approx 400$  MPa. In Stage III, instead of a stress plateau, there is a gradient in the stress–strain curve similar to a work-hardening response. Upon unloading, the reverse transformation proceeds in two steps. The underlying transformation path through the three stages is interpreted based on the evolution of the inset full-field strain contours in Fig. 2, which are calculated using *in situ* DIC. In the

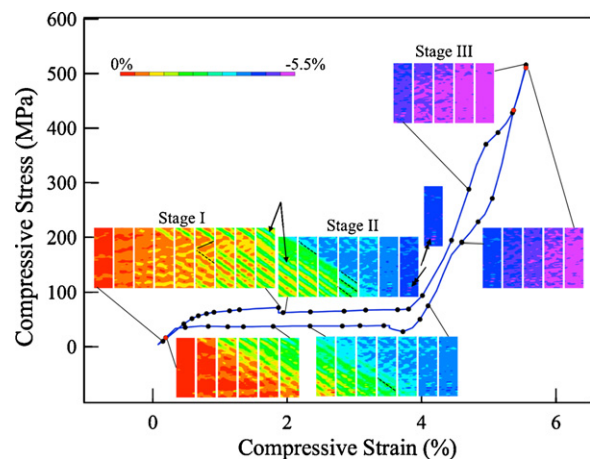


**Fig. 2.** Pseudoelastic response in Fig. 1 with inset images showing the DIC full-field strain contours that expose the transformation path. The inset images represent a  $3.2\text{ mm}$  (vertical)  $\times$   $1\text{ mm}$  (horizontal) area. Each image corresponds to a black dot along the stress–strain curve. Within the inset, the dashed and solid lines delineate two variants: dashed-variant 1 and solid-variant 2. The arrows point out local strain islands which are explained in the text.

following, the transformation morphology is described followed by an interpretation of the underlying inter-martensitic path.

Stage I proceeds via band formation from Fig. 2. Initially, horizontal bands (orange) form nearly perpendicular to the loading direction (vertical). Near the critical transformation stress, new bands (yellow) form. In the sixth image, it is evident that these bands are oriented differently with respect to the loading direction (indicated by dashed lines). The strain grows for one orientation, resulting in multiple bands (green) with increasing deformation up to the drop in stress. The region between the green bands is predominantly yellow, and thus, the other bands grow and coalesce up to the stress peak. Furthermore, localized regions within the green bands exhibit strains as high as  $-3.7\%$ , which is substantially higher than the  $-2\%$  macro-scale strain (extensometer measurement). The  $-3.7\%$  corresponds to the turquoise strain contour, the intermediate color between green and light blue.

When the stress drops and Stage II ensues, a phase boundary (marked by a dashed line) can be seen in the upper right corner of the first inset image in Stage II. Behind the boundary are turquoise and light blue contours. Just ahead of the boundary, green bands coalesce. Within green bands, turquoise contours (highlighted by the arrow in Fig. 2) are present and local strains reach  $-3.7\%$ . The boundary propagates with increasing strain and the aforementioned observations prevail. In the fourth image in Stage II the image exhibits a heterogeneous character. The area is primarily light blue with turquoise regions which vary in size spatially and appear like islands. The transformation continues in this heterogeneous manner. The last image in Stage II is predominantly blue with light blue islands. Note that a small purple region (marked by the double arrow) exists, corresponding to the maximum strain ( $-5.5\%$ ); though the macro-scale strain is only  $-4\%$ . As the load is increased, the full-field strain measurements indicated nearly uniform strain as compared to the previous images. The strain is primarily  $-4.8\%$  within the 17th image. Based on this, the microstructure change is considered complete. In the first image of Stage III purple contours become prevalent, and thus, this is considered as the onset of the final transition. The transformation morphology is heterogeneous at the second critical transformation stress. The last image during loading is primarily purple, with minute blue contours. During unloading the reverse transformation morphology mirrors that of the forward case.

Previous works report that  $A \rightleftharpoons 10M \rightleftharpoons 14M \rightleftharpoons L1_0$  is stress-induced in this class of NiMnGa SMAs [9–11]. The current results are rationalized based on this transformation sequence. The initial horizontal orange bands are peculiar as only elastic deformation is expected prior to the transformation, which would produce homogeneous deformation. The bands may be variants of  $10M$  martensite or a pre-martensitic structural transition. Based on the phase diagrams presented in Refs. [4,5] a pre-martensitic structural transition can occur for the current material. The green bands can be attributed to the growth of  $10M$  martensite, which is preferentially oriented to the external load. Because the bands are oriented differently, they can be two different variants.

The turquoise phase boundary that traverses the specimen throughout the plateau corresponds to the transition to  $14M$ . Note that the  $10M$  bands coalesce ahead of the boundary. The turquoise contours can form within the green  $10M$  bands, as pointed out in the last image of Stage I and the first image of Stage II. This transition appears to be heterogeneous. By contrast, our previous study showed that an inter-martensitic transformation facilitated the propagation of a single interface with a uniform contour behind the boundary [16]. In the current case, we propose that the boundary propagates by a different mechanism. Because the turquoise contours are observed within green bands, Stage II likely corresponds to detwinning of  $10M$  martensite and  $10M \rightarrow 14M$ . This is illustrated in the fourth image of Stage II. The dashed lines out-

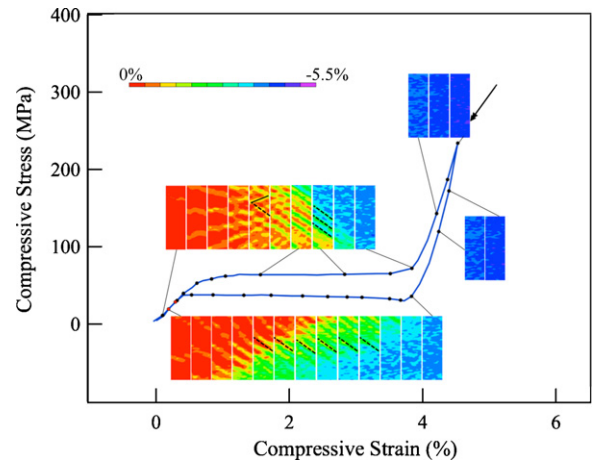


Fig. 3. The pseudoelastic response after 15 cycles at room temperature. The inset *in situ* DIC images show the transformation path throughout Stages I and II (compare Fig. 2). Each image corresponds to a dot along the stress–strain curve. The dashed and solid lines delineate the same two variants observed in Fig. 2.

line the green bands and turquoise areas are present between the bands or variants. As detwinning and the inter-martensitic conversion occur concomitantly, the strain contours are heterogeneous behind the interface. Based on the current results, the maximum strain for the  $10M$  is  $-4.1\%$ .

Lüders-like deformation is associated with the inter-martensitic transformation  $10M \rightarrow 14M$ . To nucleate the  $14M$  structure requires a higher stress than the stress required to complete the transition throughout the untransformed material. A lower driving force, i.e. stress, is required to propagate the transformation in the remaining volume fraction of material once the  $14M$  habit plane exists [17]. The conversion to  $14M$  is complete in the 17th image, and thus the blue contour is uniform as compared to the preceding strain fields. The  $14M$  martensite exhibits a maximum strain near  $-4.5\%$ . In Stage III, the  $14M$  structure converts to  $L1_0$ . Stage III can be considered a heterogeneous nucleation and growth for the  $14M \rightarrow L1_0$  inter-martensitic transition. The transformation strain is less than  $-1\%$ , which agrees with the theoretical predictions in Ref. [10]. For this transition, however, the stress–strain response exhibits a hardening like response. In summary, the modulated to modulated conversion  $10M \rightarrow 14M$  occurs in Stage I and Stage II and the modulated-to-non-modulated transition  $14M \rightarrow L1_0$  occurs in Stage III.

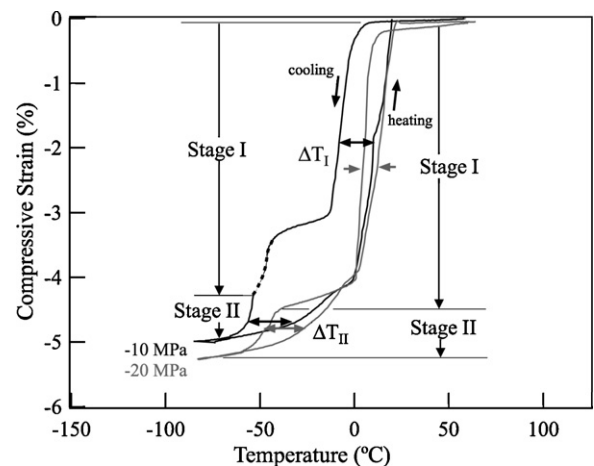
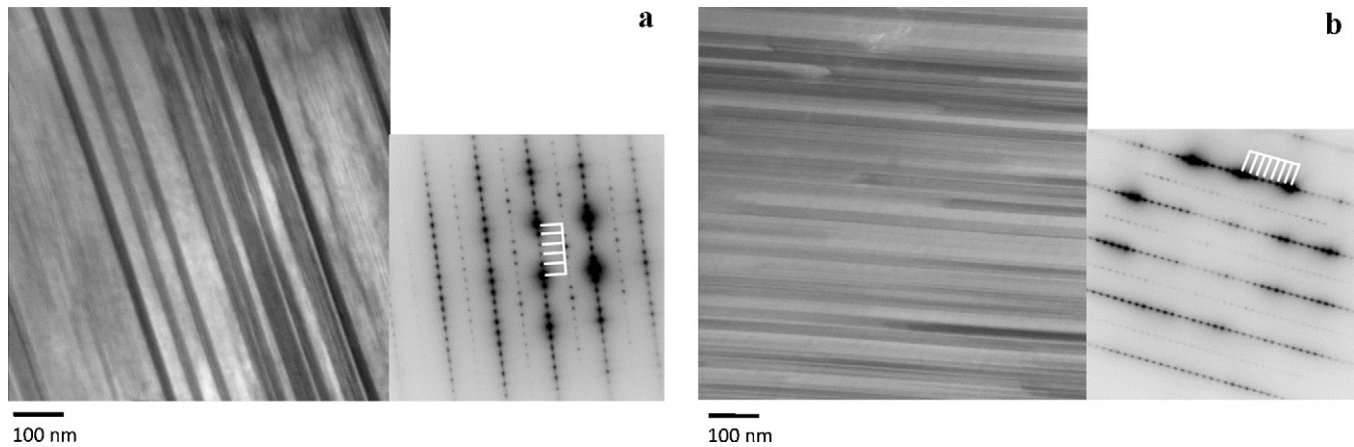


Fig. 4. The strain–temperature responses for unaged  $\text{Ni}_{53}\text{Mn}_{22}\text{Ga}_{25}$  [001] oriented single crystal under constant compressive load. Two stages are rationalized in the next. The dashed section in Stage I at  $-10$  MPa is explained in the text. Horizontal arrows mark the thermal hysteresis  $\Delta T$ .



**Fig. 5.** a. TEM showing the fine lamellae corresponding to 10M martensite. The corresponding diffraction pattern is shown to the right; the white lines delineate 5-period modulation. b. TEM showing the fine lamellae corresponding to 14M martensite. The corresponding diffraction pattern is shown to the right; the white lines delineate 7-period modulation. This sample has been trained with application of 10 cycles at 50 °C at  $-3\%$  strain.

**Fig. 3** shows the meso-scale full-field strain evolution after cycling. Here, the transformation is a single stage based on the DIC strain measurements. The stress-drop observed in **Fig. 2** is no longer present. Instead the transformation occurs at a plateau stress near 64 MPa, which is approximately equal to the plateau stress in the initial cycle (**Fig. 1**). *In situ* measurements expose that the underlying mechanism is the same as those observed in Stages I and II from **Fig. 2**. Furthermore, the same variants 1 and 2 (dashed and solid lines in **Fig. 3**) can be identified after cycling. A boundary does not appear to propagate after cycling. Instead, 10M variants (green bands) convert to 14M (turquoise) and coalesce. This is illustrated in the 8th image. Dashed lines highlight three bands. Between the bands, turquoise and light blue contours exist which correspond to 14M martensite.

Beyond the plateau, linear loading is observed. This is typically associated with elastic loading of martensite. In the current case, the unloading curve does not match the loading segment. Elastic unloading of martensite is not the only mechanism involved. Instead, a hysteresis exists due to irreversible mechanisms, which may arise due to deformation of 14M and a concomitant  $14M \rightarrow L1_0$  phase change. Purple regions are evident in the inset image at the peak load (marked by the double arrow). During unloading, the dashed line tracks the reversion of a martensite variant. The evolution can be attributed to the reversion to 10M and the subsequent transition from detwinned 10M to austenite. Ultimately, the results show unequivocally that the plateau stress can be observed without the motion of a single interface or single variant.

The strain-temperature responses at the constant stress levels of  $-10$  and  $-20$  MPa are shown in **Fig. 4**. At  $-10$  MPa, the forward transformation initiates at approximately  $M_s = 7^\circ\text{C}$ , which is well below the stress-free  $M_s$  temperature ( $27.5^\circ\text{C}$ ) determined from the DSC analysis. Note that the  $M_s$  for the  $-20$  MPa case is also below the stress-free  $M_s$  temperature. The undercooling reflects that a higher driving force is required to initiate the transformation. Recall that in the stress-strain case differently oriented variants were observed at the onset of loading in the *in situ* DIC images. The existence of these variants can suppress the transformation under compressive load. Two distinct stages are observed in the cooling curves. The results underscore that successive inter-martensitic transitions are thermal-induced under compressive load. In Stage I, the  $A \rightarrow 10M \rightarrow 14M$  is the predominant inter-martensitic transformation and 14M converts to  $L1_0$  in Stage II. The transformation pathway is rationalized in the following paragraph.

The maximum transformation strain in Stage I is about  $-4.5\%$  at  $-20$  MPa. The strain accrued in Stage II is approximately  $-0.7\%$  at  $-10$  and  $-20$  MPa. The strains are equivalent to those in Stages

I and II and Stage III for the stress-strain case in **Fig. 1**. The equivalent levels of strain support that in the strain-temperature case Stage I is  $A \rightarrow 10M \rightarrow 14M$  and Stage II is  $14M \rightarrow L1_0$ . The dashed section of the cooling curve at  $-10$  MPa highlights that Stage I exhibits multiple stages. Apparently, a larger volume fraction of material undergoes the  $A \rightarrow 10M \rightarrow 14M$  at  $-20$  MPa, which facilitates a single stage in Stage I. In **Fig. 4**, arrows located at half the transformation strain for Stage I mark the thermal hysteresis. The thermal hysteresis for Stage I  $\Delta T_I$  shrinks noticeably from  $18^\circ\text{C}$  to  $8^\circ\text{C}$  when the compressive stress is increased from  $-10$  to  $-20$  MPa. Similar observations have been observed for the  $A \rightarrow 10M \rightarrow 14M \rightarrow L1_0$  inter-martensitic transformation in NiFeGa single crystals [17]. The smaller hysteresis is attributed to an increasing in elastic strain energy owing to the inter-martensitic transition. Energy dissipation may be curtailed as the  $10M \rightarrow 14M$  transition becomes predominant. For Stage II, the thermal hysteresis  $\Delta T_{II}$  is equivalent at  $-10$  and  $-20$  MPa. This substantiates the  $14M \rightarrow L1_0$  transition at both stress levels.

The stress-strain (**Fig. 1**) and strain-temperature (**Fig. 4**) curves show stark contrasts between the first two stages and the third stage. The stress hysteresis ( $\Delta\sigma_2 \approx 130$  MPa) for Stage III is four times larger than that of Stages I and II ( $\Delta\sigma_1 \approx 30$  MPa). The thermal hysteresis at  $-20$  MPa for Stage III ( $23.4^\circ\text{C}$ ) is nearly three times larger than that for Stages I and II ( $8^\circ\text{C}$ ). The differences are due to the dissimilar underlying mechanisms in the transformation paths. Initially there is a transition between the modulated crystal structures 10M and 14M. The successive transition  $14M \rightarrow L1_0$  is from a modulated to a non-modulated structure. This transition must facilitate more severe dissipation compared to the inter-modulated one. TEM images in **Fig. 5** show that 10M and 14M martensite forms fine martensite twins, which may promote energy storage and lower the hysteresis.

#### 4. Conclusions

This investigation elucidates the inter-martensitic transformation path for an  $[001]$  oriented single crystal  $\text{Ni}_{53}\text{Mn}_{22}\text{Ga}_{25}$  loaded in compression. The stress-induced inter-martensitic transformation path  $A \rightarrow 10M \rightarrow 14M \rightarrow L1_0$  has been reported based on macro-scale extensometer measurements [10,11]. In the current study, *in situ* DIC measurements yield the evolution of meso-scale, full-field strain contours. Based on the meso-scale evolution, the morphology for  $A \rightarrow 10M \rightarrow 14M$  (modulated-to-modulated) contrasts that observed for  $14M \rightarrow L1_0$  (modulated-to-non-modulated). As a result of the inter-martensitic transformations, the stress-strain

and strain–temperature responses exhibit multi-stages. This work supports the following conclusion.

1. In the room temperature stress–strain response, the underlying transformation morphology exhibits three stages. Stage I is  $A \rightarrow 10M$ , which occurs via band formation. This martensitic transformation requires continually increasing compressive stress levels due to the interaction of multiple martensite variants. With increasing stress, mainly two variants are preferentially oriented to the applied load.
2. After the stress reaches a maximum, the stress drops and Stage II ensues. The inter-martensitic transition  $10M \rightarrow 14M$  takes place. A single boundary traverses the specimen over a plateau stress. Though a single-interface is observed, *in situ* DIC reveals evidence of mainly two-variants. The variants appear to be the same as those observed in Stage I.
3. The critical transformation stress for Stage III is 340 MPa higher than that of Stage I. The transformation is attributed to  $14M \rightarrow L1_0$ . Neither bands nor phase boundaries are evident, and the path is considered heterogeneous nucleation and growth. The macro-scale extensometer measurements show a work hardening like response. A larger driving force must facilitate nucleation of  $L1_0$  from  $14M$ , and thus higher stress levels are required to continue the transformation in a larger volume fraction of material.
4. After deformation cycling, Stages I and II are indistinguishable and a stress-drop is not observed. Remarkably, the *in situ* DIC analysis reveals that the underlying transformation path is equivalent.
5. The strain–temperature response confirms that inter-martensitic transformation  $A \rightleftharpoons 10M \rightleftharpoons 14M$  is thermally induced under constant compressive load, which produce two stages in the cooling strain–temperature curve:  $A \rightarrow 10M \rightarrow 14M$  and  $14M \rightarrow L1_0$ . The transformation strains match those observed for the corresponding transformations in the stress–strain response.
6. A dual hysteresis is observed in the room temperature stress–strain response, as well as the strain–temperature response. The modulated-to-modulated transition  $A \rightleftharpoons 10M \rightleftharpoons 14M$  for Stages I and II facilitates a smaller stress hysteresis than the modulated-to-non-modulated transition  $14M \rightarrow L1_0$  in Stage III. For the stress–strain case, single interface motion, promotes lower energy dissipation compared to heterogeneous nucleation and growth for  $14M \rightarrow L1_0$ . In the strain–temperature case, the inter-martensitic transition  $A \rightleftharpoons 10M \rightleftharpoons 14M$  becomes prevalent with increasing constant stress and the thermal hysteresis shrinks.

## Prime novelty statement

The uniqueness of this work is that the underlying stress-induced transformation mechanism in a single crystalline NiMnGa shape memory alloy is clarified utilizing *in situ* digital image correlation. Furthermore, we investigate the response after cycling to ascertain the influence of stabilization on the mechanism. The findings challenge traditional rationale for the stress plateau observed in the pseudoelastic response of SMAs.

## Acknowledgements

The work received support from NSF under CMMI 09-26813. The authors would like to acknowledge Yuri Chumlyakov from the Siberian Physical Technical Institute, Tomsk, Russia for providing the single crystals and fruitful discussions.

## References

- [1] K. Ullakko, J.K. Huang, C. Kantner, R.C. O'Handley, V.V. Kokorin, Applied Physics Letters 69 (1996) 1966–1968.
- [2] O. Hezcko, Journal of Magnetism and Magnetic Materials 290–291 (2005) 787–794, Part 2.
- [3] J.D. Callaway, H. Sehitoglu, R.F. Hamilton, K. Aslantas, N. Miller, H.J. Maier, Y. Chumlyakov, Applied Physics Letters 89 (2006) 221901–221905.
- [4] P. Entel, V.D. Buchelnikov, M.E. Gruner, A. Hucht, V.V. Khovailo, S.K. Nayak, A.T. Zayak, in: Advances in Shape Memory Materials: Magnetic Shape Memory Alloys, Trans Tech Publications Ltd, Laubisrutistr. 24, Stafa-Zuerich, CH-8712, Switzerland, 2008, pp. 21–41.
- [5] A. Planes, L. Manosa, M. Acet, Journal of Physics: Condensed Matter 21 (2009) 233201–233229.
- [6] V.A. Chernenko, E. Cesari, V.V. Kokorin, I.N. Vitenko, Scripta Metallurgica et Materialia 33 (1995) 1239–1244.
- [7] J. Pons, V.A. Chernenko, R. Santamarta, E. Cesari, Acta Materialia 48 (2000) 3027–3038.
- [8] C. Seguí, V.A. Chernenko, J. Pons, E. Cesari, in: International Conference on Martensitic Transformations, 10–14 June 2002, EDP Sciences, France, 2003, pp. 903–906.
- [9] V.V. Kokorin, V.V. Martynov, V.A. Chernenko, Scripta Metallurgica et Materialia 26 (1992) 175–177.
- [10] V.V. Martynov, V.V. Kokorin, Journal de Physique III (Applied Physics, Materials Science, Fluids Plasma and Instrumentation) 2 (1992) 739–749.
- [11] Y. Cui, L. Wu, S. You, J. Zhang, Z. Wu, C. Kong, J. Chen, G. Wu, Solid State Communications 149 (2009) 1539–1542.
- [12] R.F. Hamilton, H. Sehitoglu, C. Efstathiou, H.J. Maier, Acta Materialia 55 (2007) 4867–4876.
- [13] M.A. Sutton, W.J. Wolters, W.H. Peters, W.F. Ranson, S.R. McNeill, Image and Vision Computing 1 (1983) 133–139.
- [14] T.C. Chu, W.F. Ranson, M.A. Sutton, W.H. Peters, Experimental Mechanics 25 (1985) 232–244.
- [15] M.A. Sutton, C. Mingqi, W.H. Peters, Y.J. Chao, S.R. McNeill, Image and Vision Computing 4 (1986) 143–150.
- [16] C. Efstathiou, H. Sehitoglu, J. Carroll, J. Lambros, H.J. Maier, Acta Materialia 56 (2008) 3791–3799.
- [17] R.F. Hamilton, H. Sehitoglu, K. Aslantas, C. Efstathiou, H.J. Maier, Acta Materialia 56 (2008) 2231–2236.